The Astrophysical Journal, 873:125 (7pp), 2019 March 10 https://doi.org/10.3847/1538-4357/ab04a4

Evidence for the Two-fluid Scenario in Solar Prominences

E. Wiehr[1], G. Stellmacher[2], and M. Bianda[3]
[1] Institut für Astrophysik, D-37077 Göttingen, Germany; ewiehr@gwdg.de
[2] Institut d'Astrophysique, F-75014, Paris, France; stell@iap.fr
[3] Istituto Ricerche Solari Locarno, associated with Università della Svizzera italiana, Ch-6605 Locarno, Switzerland; mbianda@irsol.ch
Received 2018 November 30; revised 2019 February 2; accepted 2019 February 4; published 2019 March 12

Abstract

This paper presents observational evidence of the different dynamical behavior of neutral and ionized species in solar prominences. The analysis of a time-series of Sr II 4078 Å and Na *D* spectra in a quiescent prominence yields systematically larger Doppler shifts (line-of-sight velocities) for the ions $V_{\rm LOS}({\rm Sr\,II}) = 1.22 \times V_{\rm LOS}({\rm Na}\,D)$. Both lines show a 30 minute oscillation of good coherence. Sixteen hours later the same prominence underwent marked morphological changes (with a rising dome), and the Sr II velocity excess dropped to $V_{\rm LOS}({\rm Sr\,II}) = 1.11 \times V_{\rm LOS}({\rm Na}\,D)$. The same excess is found for the line pair Fe II 5018 Å and He I 5015 Å. The widths of the ionic lines, mainly non-thermally broadened, are not related to the macro-velocities. The emission ratio of Na *D* and Sr II, a measure of the electron density, yields $n_{\rm e} = 4 \times 10^{10}\,{\rm cm}^{-3}$, shows no relation with the $V_{\rm LOS}$ variation or with height above the limb, and seems to be reduced 16 hr later during the active phase. We apply a new wavelength reference from aureola spectra, which is independent of photospheric velocity fields.

Key words: methods: observational – Sun: filaments, prominences – techniques: spectroscopic

1. Introduction

The different dynamical behavior of neutral and ionized species has been receiving increasing attention recently. It can be studied in solar prominences because, due to their relatively low temperature of $T \leqslant 10^4$ K, they represent a partially ionized and weakly collisional plasma with a considerable number of neutrals (e.g., Gilbert et al. 2002). Numerical simulations indicate that the decoupling of neutral and ionized species in the solar atmosphere can give rise to non-ideal MHD effects that can result, for instance, in heating caused by the friction between the two species, modify the equilibrium of magnetic structures, introduce instabilities under certain magnetic configurations, or change the way the various wave modes transform into each other and propagate through the atmosphere (see the review by Ballester et al. 2018).

Motivated by these considerations different observers tried to measure differences between the line-of-sight (LOS) velocities of ions and neutrals. From simultaneous time-series spectra, Anan et al. (2017) found no conclusive differences, whereas Khomenko et al. (2016) found differences only at restricted locations with high velocities in short-lived transients. Stellmacher & Wiehr (2017), on the contrary, found systematically larger LOS velocities for ions (Sr II, Fe II) than for neutral atoms (Na I and He I), whereas a comparison between neutrals (H, He) gives a 1:1 relation. The conspicuous similarities between the spectra of Sr II 4078 and Na *D* suggest that these lines share the same dynamical behavior within a common resolution element (in those data about $1\farcs5 \times 1\farcs5$). In order to investigate this behavior in more detail, we discuss new observations of the faint metallic lines Sr II 4078 and Na *D*. These are optically thin and can be expected to respond quite selectively to "hot" or "cold" plasma conditions because Sr ionizes above ≈9000 K, where neutral Na hardly exists.

2. Observations

From the Locarno observatory (IRSOL) we observed a quiescent prominence at the west limb, 5° north, on 2017 June 24–26. Its appearance on June 24 as a disk filament shows that the prominence is inclined to the limb by ≈45° (Figure 1). The two emission lines Sr II 4077.71 Å and Na D_2 5889.95 Å are taken in the 13th and 9th orders, respectively, at a fixed grating angle. A simple change of two pre-filters separating the orders allows monitoring of both lines at almost the same position on the CCD (Figure 2).

The unchanged grating angle allows measurement of the aureola spectra (giving the parasitic light superposing the emission lines) immediately before and after the prominence spectra. In our former sequential observations (Stellmacher & Wiehr 2017), the change of the grating angle between the Sr II and the Na *D* exposures required repeatedly expose aureole spectra and thus alternating the telescope pointing between the prominence and its (emission-free) neighborhood. This method is sensitive to the pointing accuracy and typically requires a time interval of several minutes between the observation of both lines.

In the present observations the repetition rate is much shorter due to a 1.5 s switch of the two pre-filters. The dimension of the camera chip allows coverage of both Na *D* lines. For comparison with former data, we additionally observed on June 26 the neighboring emission lines He I 5015 Å and Fe II 5018 Å, and, separately, H_δ 4101 Å. Precise guiding is assured by the accurate monitoring of the Gregory telescope's primary image (Küveler et al. 2003).

Disk center spectra are not used for wavelength references but rather to calibrate the line intensity in absolute units (erg/(s cm^2 ster)), using the tables by Labs & Neckels (1970). The spectrograph slit of correspondingly $1\farcs5$ width and 120″ length was oriented along the direction of refraction (i.e., toward zenith).

2.1. Refraction in Earth's Atmosphere

When comparing spectral lines with a marked wavelength difference (here, 1818 Å between Sr II and Na D_1), the spectrograph slit must be precisely oriented along the direction of refraction to ensure that identical solar structures occur in

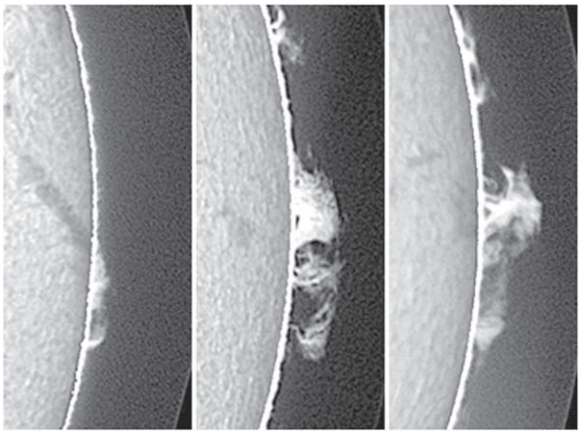

Figure 1. Prominence W5N on June 24 (Learmouth; left), 25 (Big Bear; middle), 26 (Udaipur; right panel); north is up, west is right.

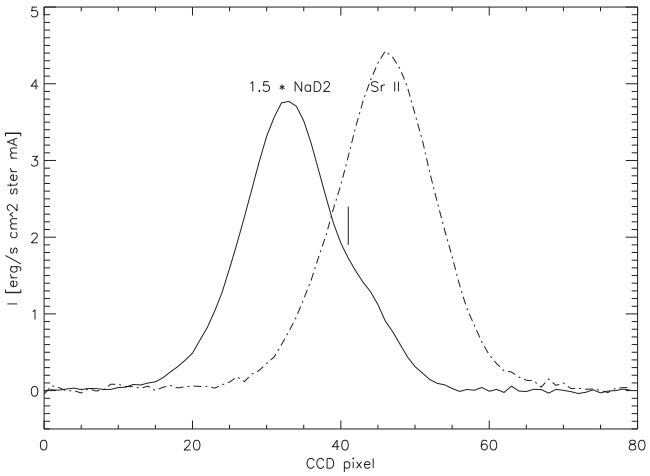

Figure 2. Emission lines Na D_2 5889.95 Å (9th; 8.4 mÅ px^{-1}) and Sr II 4077.71 Å (13th order; 5.8 mÅ px^{-1}) at a fixed grating angle yielding neighboring locations on the CCD; the H_2O 5890.7 Å blend in the red wing of Na D_2 is indicated by a vertical bar.

both spectra (shifted perpendicular to the dispersion). This is obtained by orienting the slit along the zenith direction, which, however, rotates over the solar image. As a consequence, a slit oriented toward the zenith sweeps through the solar structures.

The daily variation of the parallactic angle Φ (spanned by the geographic north and zenith direction) depends on the solar decl. $D_{\rm Sun}$ (Figure 3). For $D_{\rm Sun} \geqslant 0°$, Φ shows a minimum and a maximum, respectively, at sunrise and at sunset. With increasing $D_{\rm Sun}$ these extrema become broader and move apart from the sunrise and the sunset. For $D_{\rm Sun} > 20°$ (May 20 through July 20) and the 46.°17 latitude of IRSOL, the two flat extrema allow orientation of the spectrograph slit at hour angles $-6.0 < \alpha < -3.3$ hr and $+3.3 < \alpha < +6.0$ hr such that it deviates from the zenith direction by $\leqslant \pm 1°$ (two dotted horizontal lines in Figure 3). This allows time-sequence observations up to 2.7 hr with an extended slit always covering the same solar structures.

Balthasar & Wiehr (1994) made use of the complete morning minimum for simultaneous observation of Ca II 8498 Å and the line pair He 3888 Å and H_8 3889 Å in a quiescent prominence. Anan et al. (2017) observed a similar spectral range of almost 4600 Å from 10:53 to 11:37 local time, where Φ varies considerably. Here, we present observations of Sr II and Na D

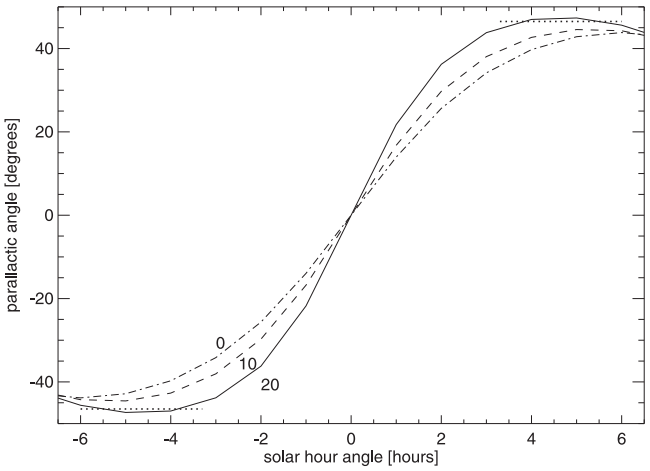

Figure 3. Parallactic angle Φ as a function of solar hour angle for the Locarno observatory (at 46°17 latitude) and solar declinations $D_{\rm Sun} = 0°$ (dash-points), $D_{\rm Sun} = +10°$ (dashes), $D_{\rm Sun} = +20°$ (full line); observing windows have Φ≈const. (dotted horizontal lines).

in a prominence on June 25, during the afternoon maximum and 16 hr later on June 26, during the morning minimum with a slit orientation toward zenith.

3. Data Reduction

Prominence emission lines are superposed by parasitic light originating from imperfect telescope optics (rather than from Earth's atmosphere; see Stellmacher & Wiehr 1970). We take spectra of the "aureola" in the immediate (emission-free) prominence neighborhood with almost the same slit inclination to the solar limb. The obtained aureole spectra are normalized to the intensity of the prominence background and then subtracted (for details see Ramelli et al. 2012). These do not allow full disappearance of the terrestrial H_2O lines by subtraction. (The reason for this is discussed in Section 3.1.) In particular, remnants of H_2O 5890.7 Å affect the red wing of Na D_2 (Figure 2). For comparison with Sr II we thus prefer Na D_1, which is not affected by terrestrial H_2O lines. We verify that both Na D lines have the same Doppler shifts, and that their integrated line intensities show a fixed relation $D_2/D_1 = 1.4$ (in agreement with Landman 1981).

We spatially average the spectra over five rows (1.″7) adapted to the spectrograph slit of correspondingly 1.″5 width. For the spatial regions, visually selected to avoid multi-component emissions and marked in Figures 5(b) and 6(b), we determine macro-shifts, $V_{\rm LOS}$, reduced widths, $\Delta\lambda_D/\lambda_0$, and integrated line intensities, $E = I_0 \times \Delta\lambda_D \times \pi$ (valid for optically thin lines) fitting single Gaussians sequentially to the upper 15%, 40%, or 65% of the central intensity. The wavelengths of the emission maxima are determined from the upper 15%. Reduced widths and integrated intensities are only taken from narrow and symmetric line profiles, where the Gaussians at 15%, 40%, or 65% of the central intensity are almost identical. This criterion excludes asymmetric profiles; multi-peak profiles are already avoided visually (see above).

3.1. Scaling the Wavelengths

As a wavelength reference for Doppler shifts we determine the centers of the Sr II and Na D absorption lines in the aureola at the upper ends of each spectrum at 115″ from the limb in slit direction (which corresponds to 80″ above the equatorial west

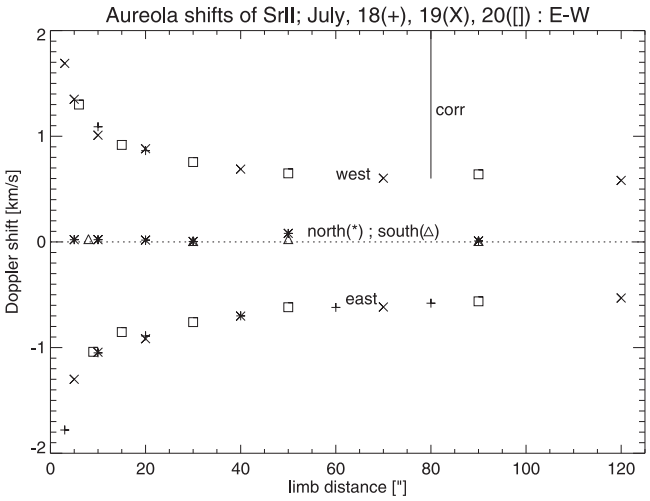

Figure 4. Doppler shift of Sr II in the aureola as a function of distance from the limb, eastward and westward of the solar equator and northward and southward of the solar poles; the correction to a co-rotating reference is indicated.

limb accounting for the slit inclination). This reference allows calibration of Doppler shifts independent of the complex photospheric velocity fields at disk center and of ubiquitous drifts of the spectrograph.

In order to connect these wavelengths from the aureola to those at the solar disk, we observe (in 2018 July) aureola spectra of Sr II 4078 Å and Na D_1 at various distances from the limb. We find that the absorption lines in the aureola become increasingly blue and redshifted when approaching the east and west limbs respectively. At the solar poles, these shifts disappear (Figure 4).

The Doppler shifts in the aureola spectra are found to be equal for the Sr II and the Na D line. Their variation along the slit is the same in the aureola and in the emission spectra because the slit inclination is largely preserved. The different colors of both lines indeed affect the aureole continuum intensity, which is considered by normalization.

Figure 4 indicates that aureola regions closer to the solar disk obtain parasitic light from increasingly smaller segments of the solar sphere, which thus imprint increasing rotational Doppler shifts (they are evidently equal for the Na and Sr II lines) on the respective aureola spectra. On the other hand, for increasing limb distances, the aureola contains parasitic light from increasingly larger segments, and finally from the half-sphere with a much smaller mean rotational Doppler shift. Near the poles the sphere segments contain no rotational Doppler shifts, and the wavelengths in the aureola then show zero shifts for all limb distances (Figure 4). Hence, the polar aureola gives an almost perfect standard for the calibration of Doppler velocities.

3.2. The Co-rotating Reference System

Our wavelengths from the upper end of each spectrum (80″ above the limb) may be converted to a co-rotating system. Figure 4 gives for $x = 80''$ a shift of $y = 0.6$ km s^{-1} with respect to the un-shifted polar wavelengths. Assuming 2 km s^{-1} rotation, our velocity scale had to be shifted by -1.4 km s^{-1} (marked in Figure 4) to relate it to the photosphere below the prominence.

Since we determine the aureola wavelengths of Sr II 4078 and of NaD at each spectrum of the time series, the resulting

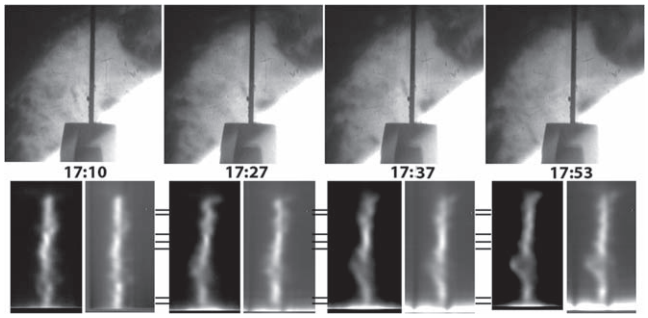

Figure 5. Prominence from June 25 at west 5°N. Upper panels: H_α slit-jaw images at time steps 1, 20, 40, 60; the slit is oriented along the direction of refraction. Lower panels: corresponding spectra of Sr II (left) and Na D_2 (right of each pair); spatial length = 65″ and the bars give the locations of scan rows.

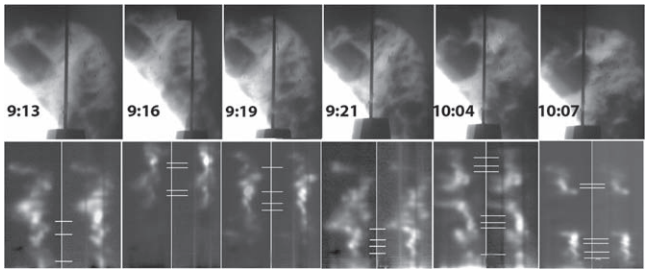

Figure 6. Same as Figure 5, but 16 hr later.

macro-velocities are free from spectrograph drifts and from slow terms of spectrograph seeing. The low noise level of the emission lines (see examples in Figure 2) and the Gaussian fit of the upper 15% lead to an estimated accuracy of $\leqslant$50 m s^{-1} for the macro-velocities.

4. Results

The H_α slit-jaw images from June 25 show that the prominence appeared quiet without noticeable morphological changes during the 42.7 minute time-series (Figure 5). In contrast to the slit-jaw images, the aspect of the spectra (lower panels of Figure 5) varies at locations with multi-component emissions, e.g., at the border of the small emission gap in the prominence center. Such multi-components become particularly visible in narrow lines from heavy elements ($\mu_{Sr} = 86.7$) and are often hidden in broad Balmer lines. We select seven spatial scan positions (marked in the lower panels of Figure 5) at regions largely free from multi-components.

On June 26, (16 hr after the June 25 observations) the prominence is less quiet and characterized by an expansion of the central emission gap, which suddenly rose up with a projected motion of $\approx$10 km s^{-1} (between 10:04:10 and 10:07:08; see the upper panel of Figure 6). This value is close to the one found by Stellmacher & Wiehr (1973) for a similar event, which also showed large Doppler shifts $\leqslant$10 km s^{-1} at the boundary of the rising cavity. Our spectra even reach 35 km s^{-1}. Yet, Sr II and Na D show striking similarity (see the lower panels of Figure 6), suggesting a common origin within the same resolution element, which we estimate to be 2″ × 2″, or 1500 km × 1500 km on the Sun.

4.1. Balmer Brightness

H_δ was only observed on June 26. We find a mean integrated intensity $E(H_\delta) = 8350$ erg/(s cm^2 ster) that, following the

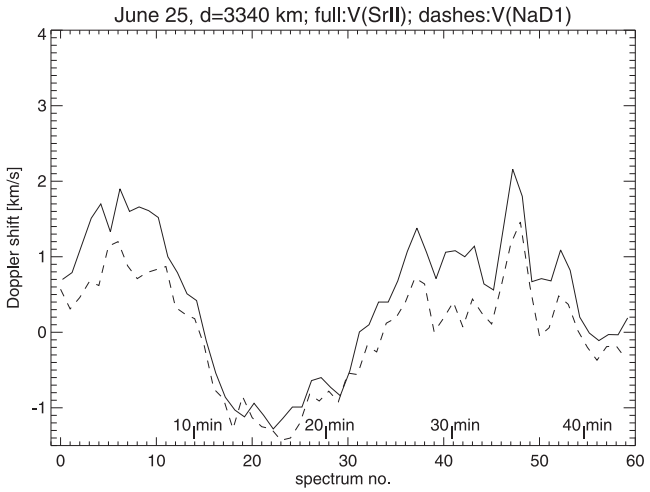

Figure 7. Velocity variation of Sr II (full line) and Na D_1 (dashes) velocities with respect to the photosphere beneath the prominence for the 60 steps of the time-series from June 25 in the lowest scan row at $d = 3340$ km from the solar limb in the slit direction.

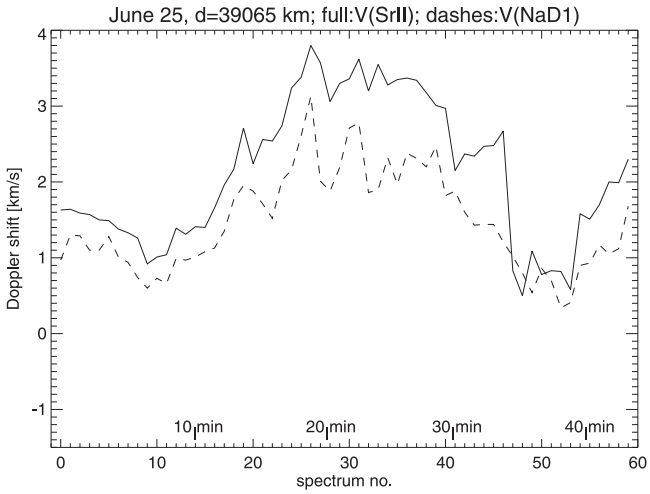

Figure 8. Same as Figure 7 but for the uppermost scan row at $d = 39{,}065$ km from the solar limb in the slit direction; the ordinate scales of Figures 7 and 8 are made equal for a direct comparison.

tables by Gouttebroze et al. (1993), for $T = 8000$ K corresponds to $\tau_\delta = 0.08$. For June 25 we estimate the H_δ emission assuming an enhancement of 3.8 with respect to June 26, for which we measured Na D_1, and obtain $\tau_\delta = 0.15$. The H_δ line is thus optically thin on both days.

For H_α the tables give $\tau_\alpha = 4.0$ and 9.5, respectively, and $E(H_\alpha) = 23$ and 38×10^4 erg/(s cm^2 ster). Assuming an elementary volume $E(H_\alpha) = 1 \times 10^4$ erg/(s cm^{2}ster) (see, Stellmacher & Wiehr 2000, and references therein) the resolution area covers, 23 and 38. Even the larger number is compatible with a single layer of $\phi \leqslant 240$ km elements in the line of sight and favors the single line approximation as in Stellmacher & Wiehr (2017). The spectra show, indeed, moments where narrower lines coincide with higher line-center intensities, as expected from the relation $E = I_0 \times \Delta\lambda_D \times \pi$ for optically thin lines.

4.2. Time Variation of the Doppler Shifts

Figures 7 and 8 show the $V_{\rm LOS}$ obtained from Sr II and Na D_1 for the 60 spectra of the time-series in the lowest and the highest scan rows on June 25 (marked in Figure 5). They are located at 3860 km and at 39,600 km from the solar limb in the slit direction. The time-series (Figures 7 and 8) shows a wave-like velocity variation with a period of ≈30 minutes for both lines. The $V_{\rm LOS}$ are synchronous in Sr II and Na D_1 with phase shifts smaller than the 42.7 s time step, and their amplitudes and means are systematically higher for Sr II than for Na D_1. In Figure 9 we compare the Sr II velocities at lower, middle, and upper locations in the prominence on June 25. The temporal velocity mean indicates an increase from 0.4 via 1.5 to 2.1 km s^{-1} through the three levels, whereas the oscillation amplitude remains almost constant. This indicates that the oscillation is superposed on an general redshift, which increases with height. The oscillation extrema move along the slit direction with 20–40 km s^{-1}.

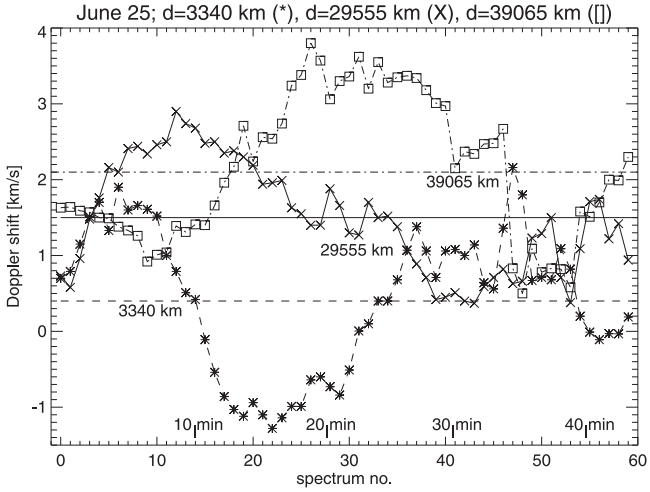

Figure 9. Time variation of Sr II velocities in the prominence from June 25, for the 60 spectra at $d = 3340$ km (dashes), at $d = 29{,}555$ km (full line) and at $d = 39{,}065$ km (dashed points) from the solar limb in the slit direction; the ordinate scale for all scans is the same as those in Figures 7 and 8.

4.3. Velocity Excess of Ions

In Figure 10, we show the scatter-plot of LOS velocities of Sr II and NaD1 in the co-rotating system (see Section 3.2) for the 60 spectra of the time series in the 7 spatial cuts (see

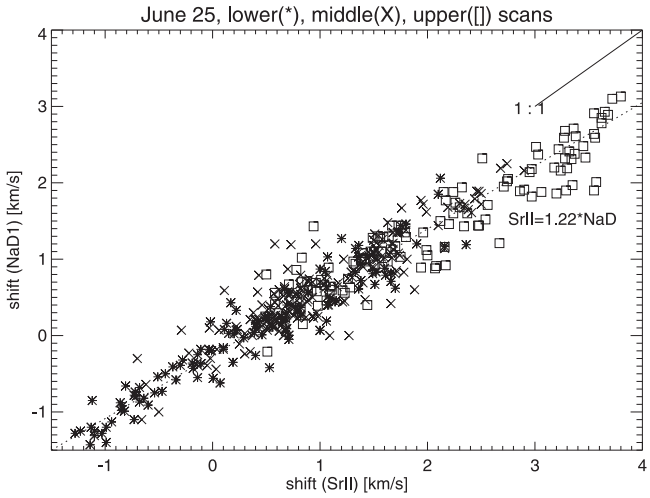

Figure 10. Scatter plot of 420 $V_{\rm LOS}$ of Sr II and Na D_1 from the 7 scan rows and 60 time steps for June 25; the plot shows that the Sr II velocities are 1.22 ± 0.01 times larger than those of Na D.

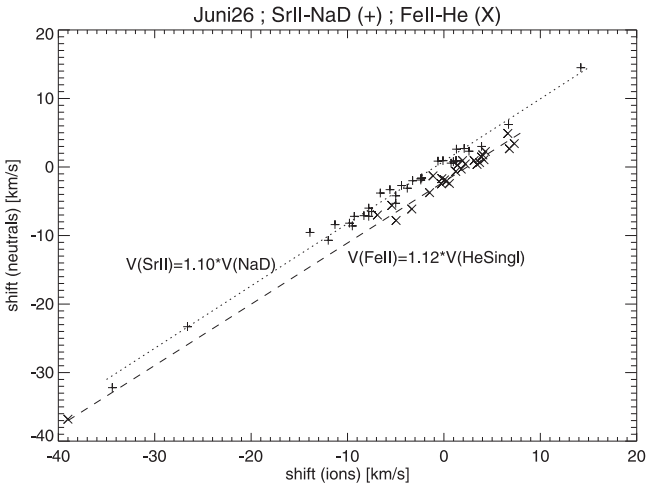

Figure 11. Scatter plot of 41 $V_{\rm LOS}$ of Sr II and Na D_1(+) and 27 $V_{\rm LOS}$ of Fe II 5018 Å and He I 5015 Å (X) for June 26; the ion velocities are 1.11 ± 0.05 times larger than those of the neutrals; the ordinate displacement of $V_{\rm LOS}$(He) reflects the missing reference wavelength in the aureola spectrum.

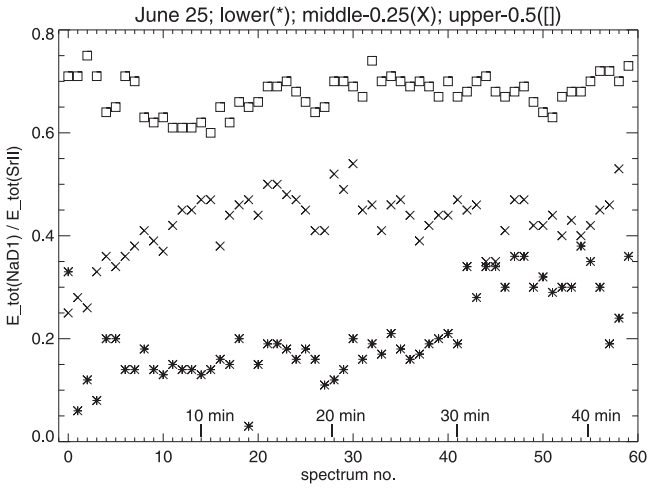

Figure 12. Emission ratio E(Na D_1)/E(Sr II) for the 60 spectra from June 25 at lower (stars), middle (X-signs), and upper locations (squares) vertically displaced by 0, −0.25, and −0.5 for clearness.

Figure 5). From these 420 spectra, we obtain a net shift excess of VLOS (Sr II) = 1.22 ± 0.02× VLOS (NaD1). Concerning the error range, we note that the Gaussian fit to the low-noise spectra (see Figure 2) will not markedly affect the accuracy. We consider the scatter in Figure 10 to be due to different influence of image motion in the quasi-simultaneous Sr II and NaD spectra.

For June 26, we find from 41 scans in the 6 spectra (Figure 6) a smaller velocity excess than on June 25, $V_{\rm LOS}$(Sr II) = 1.10 ± 0.03 × $V_{\rm LOS}$(Na D_1) (Figure 11); this sample is smaller, however, contains higher values (notably near the rising cavity; Figure 6). For the neighboring lines Fe II 5018 Å and He I 5015 Å (singlet line) we find from 27 symmetric profiles a velocity excess of $V_{\rm LOS}$(Fe II) = 1.12 ± 0.05 × $V_{\rm LOS}$(He D_1). The slight ordinate displacement relative to the Sr II–Na D data (Figure 11) may arise from the missing reference wavelength of the He line, which does not exist in the aureola spectrum and was taken from the Fe II line via the dispersion. The identical slopes for both line pairs in Figure 11 indicate that the velocity excess of ions has actually diminished 16 hr after the observation of the time-series, and that the excess is standard behavior for ions with respect to neutrals.

4.4. Integrated Line Intensities and Electron Density

The ratio of total line intensity, $E_{\rm tot}$(Na D)/$E_{\rm tot}$(Sr II), in Figure 12 does not show the 30 minute period of $V_{\rm LOS}$ (see Figures 7–9). It is thus largely independent of macro-shifts. Possible variations of smaller periods cannot be established with sufficient significance. In Figure 13 we plot the observed range of emission ratio versus the distance from the solar limb in the slit direction and obtain a constant mean of 0.68.

The ratio of total line intensity, $E_{\rm tot}$(Na D)/$E_{\rm tot}$(Sr II), allows estimation of the electron density. Converting the Na D_1 emissions into Na D_2 emissions with the factor $E(D_2)/E(D_1)$ = 1.4 (Section 3), we obtain from the mean E(Na D_1)/E(Sr II) = 0.68 ± 0.1 the value E(Na D_2)/E(Sr II) = 0.95 ± 0.1 for June 25. Applying the calculations by Landman (1983) for T = 8000 K and $V_{n\rm th}$ = 3 km s^{-1} and the correction factor 0.5 (Landman 1986), this ratio gives $n_{\rm e} = 4 \times 10^{10}$ cm^{-3}, which is the same as that found by Stellmacher & Wiehr (2017).

On June 26, the prominence shows fainter mean emissions; E(Na D_1) reduces by ≈3.8, but E(Sr II) only by ≈2.5. As a

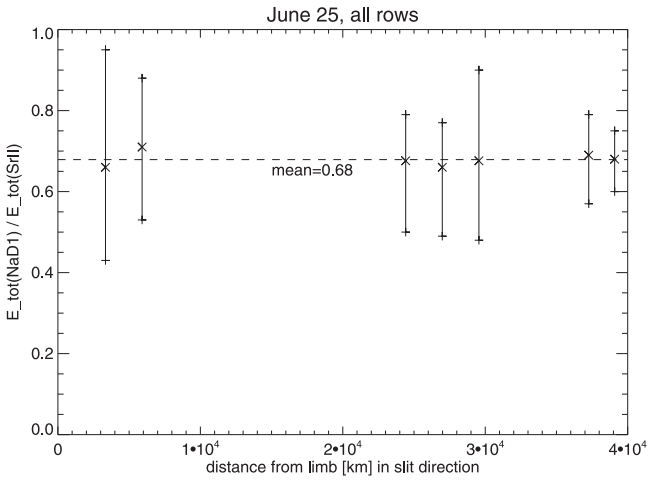

Figure 13. Mean emission ratio of Na D_1 and Sr II for all seven scan rows on June 25 as a function of distance from the limb in slit direction.

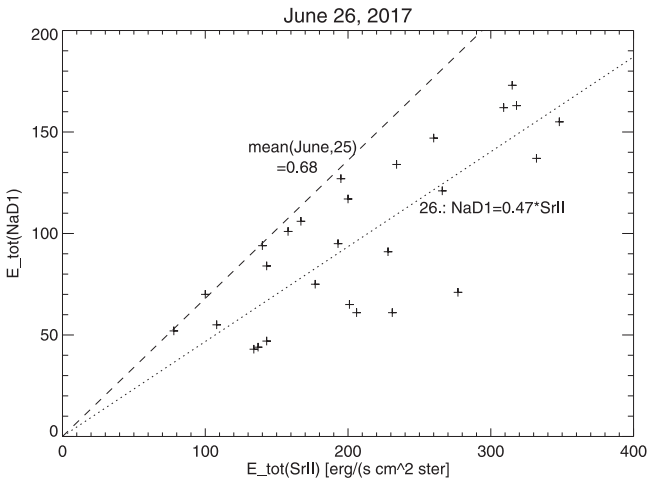

Figure 14. Relation between integrated line intensity of Na D_1 and Sr II for 28 profiles from June 26, at the spatial locations marked in Figure 6; all of them are located below the mean relation for June 25 (0.68, dashed line); the mean relation on June 26 is 0.47 ± 0.2.

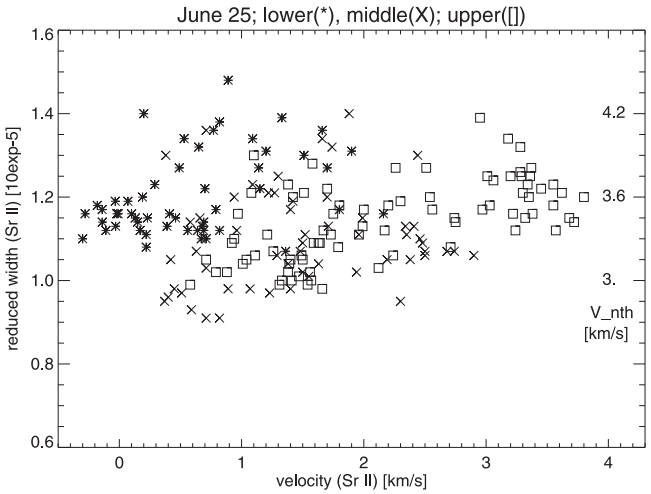

Figure 15. Relation between reduced widths and Doppler shifts of Sr II on June 25 for symmetric narrow profiles in the lower, middle, and upper scan rows (same as in Figure 9).

consequence, the mean emission ratios are generally smaller than those on June 25. The 28 line profiles, unaffected by multi-component emissions (spatial positions marked in the lower panel of Figure 6), give a wide range of emission ratios $0.25 \leqslant E(\mathrm{Sr\,II})/E(\mathrm{Na}\,D_1) \leqslant 0.7$ (Figure 14), almost entirely below the mean of 0.68 found for June 25. The range of ratios gives $1.0 < n_e < 4 \times 10^{10}\,\mathrm{cm}^{-3}$, indicating smaller n_e values on June 26 than on June 25.

4.5. Width Excess of the Sr II Line

From symmetric and narrow emissions (i.e., unbiased by multi-component emissions) we find mean reduced widths $\Delta\lambda_D/\lambda_0(\mathrm{Sr}) = 0.95 \cdot \Delta\lambda_D/\lambda_0(\mathrm{Na})$. The Doppler formula, $\Delta\lambda_D/\lambda_0 = 1/c \cdot \sqrt{2\,R\,T_{\mathrm{kin}}/\mu + V_{n\mathrm{th}}^2}$, however, leads, for the atomic mass $\mu(\mathrm{Na}) = 23$ and $\mu(\mathrm{Sr}) = 87.6$, to a markedly smaller ratio of $\sqrt{23/87.6} = 0.51$, thus indicating an excess broadening of the Sr II line. $\Delta\lambda_D/\lambda_0(\mathrm{Sr\,II})$ does not depend on the macro-velocities V_{LOS} (Figure 15). This is equally found for Na D_1, and also on June 26, even for the larger shifts occurring during the activated phase; it agrees with Envold (1972). The observed range $1.0 \lesssim \Delta\lambda_D/\lambda_0 \lesssim 1.4 \times 10^{-5}$ gives non-thermal velocities (i.e., for $T_{\mathrm{kin}} = 0$ K) of $3.0 \lesssim V_{n\mathrm{th}} \lesssim 4.2\ \mathrm{km\,s}^{-1}$.

5. Concluding Comments

5.1. The Systematic Velocity Excess of Ions over Neutrals

The data presented here confirm at higher accuracy the net drift excess of ions over neutrals observed by Stellmacher & Wiehr (2017). This systematic velocity excess differs from that of Ca II 8542 Å over He I 10830 Å, which was found by Khomenko et al. (2016) at moments of high velocities in short-lived small areas. Our result may in part be due to the judicious choice of the emission lines Sr II 4078 Å and Na D, which are optically thin and narrow, and to the fact that we analyzed a quiet prominence. The smaller velocity excess of 1.11, found for June 26, might be due to a a different degree of ionization, as is indicated from the smaller ratio of integrated line intensities (see Figure 14) or to a different density in the activated phase of the prominence.

5.2. The Electron Density

The estimate of n_e is based on the assumption that Sr II 4078 Å and Na D_2 originate in the same emission area. The visual aspects of the spectra (lower panels of Figures 5 and 6) is in favor of such a common origin. The small optical thickness ($\tau(\mathrm{H}_\delta) \leqslant 0.15$) and the small geometric extension of a single layer thickness (see Section 4) indicate a line formation in the same plasma volume. The variation of the emission ratio through the observing time (Figure 12) does not show the 30 minute variation of V_{LOS} (see Figures 7–9), indicating that the electron density n_e is not related to the macro-velocities. The constancy of n_e with height (Figure 13) is in accordance with our earlier findings (Stellmacher & Wiehr 2015, 2017). For the smaller n_e on June 26, a possible relation between the brightness decrease and/or the activation of the prominence on June 26 remains unsolved.

5.3. The Non-thermal Line-broadening

The width excess of the Sr II over the Na I profiles is in accordance with Ramelli et al. (2012) and Stellmacher & Wiehr (2015, 2017), who found emission lines from ions to be systematically broader than those from neutrals. The conjecture that this width excess may be related to the excess of ion velocities seems to not be confirmed by the results in Figure 15. Hence, the systematic width excess of lines from ions still remains unclear.

5.4. The Oscillatory Behavior of the Doppler Velocities

The time-series show a wave-like velocity variation with ≈30 minute periods, which is highly synchronous for ions and neutrals, in agreement with Balthasar et al. (1993), Balthasar & Wiehr (1994), Khomenko et al. (2016), and Anan et al. (2017). If we follow that period through the scan rows, it seems to travel along the slit direction with a velocity decelerating from $40\ \mathrm{km\,s}^{-1}$ in the lower scan rows to $20\ \mathrm{km\,s}^{-1}$ in the upper scan rows. The superposed increase of mean redshift (Figure 9) suggests a swaying motion of the prominence as a whole (see Okamoto et al. 2015). Concerning its origin, Wedemeyer et al. (2013), Hillier et al. (2013), and Wedemeyer & Steiner (2014) showed that the weak prominence magnetic field responds to ubiquitous motions of its photospheric footpoints. In this scenario, the motion of ions is directly exerted by the Lorentz force, and the motion of neutrals arises from friction with ions.

We thank Dr. R. Ramelli (IRSOL) for suggestions for data reduction and fruitful discussions, and D. Gisler (IRSOL) for developing the device to shift the pre-filters. Drs. R. Hessman (IAP Göttingen) and B. Inhester (MPS Göttingen) contributed helpful comments. E. W. and G. S. thank IRSOL for hospitality. IRSOL is supported by the Swiss Confederation (SEFRI), Canton Ticino, the city of Locarno, and the local municipalities. We are indebted to the unknown referee for carefully reading our manuscript and providing helpful hints to improve it.

References

Anan, T., Ichimoto, K., & Hillier, A. 2017, A&A, 601, A103
Ballester, J.-L., Alexeev, I., Collados, M., et al. 2018, SSRv, 214, 58
Balthasar, H., & Wiehr, E. 1994, A&A, 286, 639
Balthasar, H., Wiehr, E., Schleicher, H., & Wöhl, H. 1993, A&A, 277, 635
Envold, O. 1972, SoPh, 23, 346
Gilbert, H. R., Hansteen, V. H., & Holzer, T. E. 2002, ApJ, 577, 464

Gouttebroze, P., Heizel, P., & Vial, J.-C. 1993, A&AS, 99, 513
Hillier, A., Morton, R. J., & Erdélyi, R. 2013, ApJL, 779, L16
Khomenko, E., Collados, M., & Diaz, A. J. 2016, ApJ, 823, 132
Küveler, G., Wiehr, E., & Bianda, M. 2003, AN, 324, 308
Labs, D., & Neckels, H. 1970, SoPh, 15, 79
Landman, D. A. 1981, ApJ, 251, 768
Landman, D. A. 1983, ApJ, 269, 728
Landman, D. A. 1986, ApJ, 305, 546
Okamoto, T. J., Antolin, P., De Pontieu, B., et al. 2015, ApJ, 809, 71
Ramelli, R., Stellmcher, G., Wiehr, E., & Bianda, M. 2012, SoPh, 281, 697
Stellmacher, G., & Wiehr, E. 1970, A&A, 7, 432
Stellmacher, G., & Wiehr, E. 1973, A&A, 24, 321
Stellmacher, G., & Wiehr, E. 2000, SoPh, 196, 357
Stellmacher, G., & Wiehr, E. 2015, A&A, 581, 141
Stellmacher, G., & Wiehr, E. 2017, SoPh, 292, 83
Wedemeyer, S., Scullion, E., Rouppe van der Voort, L., Bosnjak, A., & Antolin, P. 2013, ApJ, 774, 123
Wedemeyer, S., & Steiner, O. 2014, PASJ, 66S, 10